A DIRECT SAMPLING METHOD
FOR INVERSE SCATTERING USING FAR-FIELD DATA

Jingzhi Li

Faculty of Science, South University of Science and Technology of China
Shenzhen, 518055, P. R. China

Jun Zou

Department of Mathematics, The Chinese University of Hong Kong
Shatin, Hong Kong

(Communicated by the associate editor name)

Abstract. This work is concerned with a direct sampling method (DSM) for inverse acoustic scattering problems using far-field data. Using one or few incident waves, the DSM provides quite reasonable profiles of scatterers in time-harmonic inverse acoustic scattering without a priori knowledge of either the physical properties or the number of disconnected components of the scatterer. We shall first present a novel derivation of the DSM using far-field data, then carry out a systematic evaluation of the performances and distinctions of the DSM using both near-field and far-field data. A new interpretation from the physical perspective is provided based on some numerical observations. It is shown from a variety of numerical experiments that the method has several interesting and promising potentials: a) ability to identify not only medium scatterers, but also obstacles, and even cracks, using measurement data from one or few incident directions, b) robustness with respect to large noise, and c) computational efficiency with only inner products involved.
MSC (AMS 2010): 35R30, 41A27, 78A46

1. Introduction

The capability of effectively retrieving the location and/or geometrical features of unknown scatterers from the knowledge of the scattered wave field (near-field or far-field data) is of paramount importance in many practical applications such as underground mine detection, geophysical exploration in oil industry, detection of defects or cracks in nondestructive testing, target detection using radar or sonar systems and ultrasound imaging in biomedical equipments [6, 12]. Both locations and geometrical shapes of scatterers are often the final target in the applications. Many quantitative methods have been developed for such purposes [3, 4, 12, 19, 22, 35, 36]. But there is a crucial step for these imaging processes, to find some reasonable estimated locations and shapes as their initial computational sampling domains, otherwise the imaging processes may not work or work with huge computational efforts.

A promising direct sampling method (DSM) was proposed recently in [21] to recover the inhomogeneous medium scatterers from near-field measurement data for inverse acoustic medium scattering problems. Compared with other sampling-type schemes (see, e.g., [9, 24, 32] for the detailed surveys) such as multiple signal classification (MUSIC) [8, 14, 17, 20, 34] and linear sampling method (LSM) [7, 10, 23], a distinct feature of the DSM is its capability of depicting the profile of medium scatterers using one or very few incident wave fields, through the computationally very cheap inner products of the measured data and the fundamental solution in the homogeneous background medium.

In this work, we will further explore in this direction by generalizing the DSM from the knowledge of near-field data to far-field data of the scattered waves for inverse medium and obstacle scattering problems. Extensive numerical experiments are done to investigate systematically the behavior of the DSM. An important new observation is that the DSM is able to recover not only medium scatterers, but also obstacles, and even cracks using one or two incident waves.

The full inverse scattering problem (ISP) is to determine both the shapes and the physical profiles of the scatterers, hence may require the measured data at many frequencies, not the one from a single frequency as considered in this work. It is well known that the ISP is highly nonlinear, and the first key step for the numerical treatment of a nonlinear problem is to work out a good initial guess for its approximate solution. As DSM is computationally very cheap and works with the data from only one or few incident fields, it can naturally serve as a fast, simple and effective alternative to existing numerical tools for locating a reliable approximate position of the unknown scatterers, which can then serve as a good initial guess in any existing method (see, e.g., [4, 12, 19, 22]) for achieving a more accurate estimate of the scatterer support and the inhomogeneity distribution. As we shall see numerically, the DSM can provide a very reliable location of each individual scatterer component so that one may start with a much smaller sampling region in a more accurate but computationally more demanding method. The reduction of the sizes of the initial sampling regions for unknown scatterers may save us an essential fraction of the computational efforts in the entire reconstruction process by most existing methods. Other approaches are available in the literature, which do not require an a priori good initial guess of the scatterers, e.g., the globally convergent numerical method. We refer to the monograph [5] and many references therein for the detailed description of the method and its theory for ISPs corresponding to some hyperbolic equations. Because of the time dependence, the ISPs of [5] can be considered as the ones with the data given at many frequencies.

Inverse scattering reconstruction methods using one single incident wave, or simply *one-shot* methods, date back to a long-standing open problem in the inverse scattering community, namely whether one can determine the unknown scatterer by using the near-field/far-field data from only one or several incident waves. Theoretically, the results on unique identifiability have been understood only partially, e.g., for some special classes of scatterers [12, 13], or for the class of polygonal or polyhedral scatterers [2, 15, 28, 29, 30]. Armed with the aforementioned uniqueness results, one-shot methods have been studied widely in the past few years, e.g., in [33, 16, 21, 18]. This work extends the one in [21] to make a more systematical investigation of such a promising one-shot method applied to inverse scattering problems using near-field or far-field data for many possible cases of scatterers: obstacles, inhomogeneous media and cracks or their combinations. This study reveals

more potentials of the one-shot method and provides some physical hints to answer the pending open problem from the numerical perspective. We emphasize that the direct sampling method in the current work is based on the same indicator function as that in the orthogonality sampling method developed and studied in [33, 16], but we shall present a different approach and motivation to derive this method and justify its effectiveness, in particular removing the "smallness" assumption that is crucial to the derivation of the method in [33, 16].

The paper is organized as follows. In Section 2 a brief review of inverse scattering problems is presented, along with some useful notations and identities. Section 3 describes the mathematical motivation of the DSM using far-field data and proposes a new indicator function. Section 4 provides extensive numerical simulations to evaluate the performance of the DSM using near-field or far-field data from obstacles, media and cracks. In addition, we shall provide a physical interpretation of the DSM, and compare the major features of the DSMs using near-field and far-field data. Some concluding remarks will be given in Section 5.

2. A brief review of inverse scattering problems

In this section we shall briefly describe the time harmonic inverse obstacle and medium scattering problem using near-field or far-field measurements [11, 12]. Consider a homogeneous background space $\mathbb{R}^N$ ($N = 2, 3$) that contains some scatterer components such as obstacles or inhomogeneous media, or both, occupying a bounded domain D. Let $u^{\text{inc}} = \exp(\mathrm{i}kx \cdot d)$ be an incident plane wave, with the incident direction $d \in \mathbb{S}^{N-1}$ and the wave number k, and $u = u^{\text{inc}} + u^s$ be the total field formed by the incident and scattered fields. Then the total field u induced by the obstacles satisfies the Helmholtz equation

$$(1) \qquad \Delta u + k^2 u = 0 \quad \text{in} \quad \mathbb{R}^N \setminus D,$$

or induced by the inhomogeneous medium scatterers satisfies

$$(2) \qquad \Delta u + k^2 n^2(x)u = 0 \quad \text{in} \quad \mathbb{R}^N,$$

where $n(x)$ is the refractive index. To account for the absorbing medium, the refractive index can be modeled by the complex form

$$(3) \qquad n^2(x) = n_1(x) + \mathrm{i}n_2(x).$$

The models above describe not only time-harmonic acoustic wave propagation, but also electromagnetic wave propagation in either the transverse magnetic or transverse electric models [12, 21].

Remark 1. Note that the obstacle scatterer can be viewed as the limiting case of the medium scatterer with vanishing or singular material properties. For example, an acoustic sound-soft obstacle is a limiting case of (2) as $n_2 \to +\infty$; see, e.g., [25, Eq. (4.4)] or [26, Sect. 4]. One may also refer to [27] for the sound-hard limiting case for general dimensions. Therefore, the indicator functions derived in the sequel are applicable to both inverse obstacle and medium scattering problems, although our derivations are based only on the medium scattering case.

In the rest of this section we introduce some basic notation and fundamental functions that will be needed in the subsequent discussions. First, we define a coefficient function, $\eta = \left(n^2 - 1\right)k^2$, which characterizes the inhomogeneity of the concerned media and is supported in the scatterer $D \subset \mathbb{R}^d$. Then we define function $I = \eta u$, which is called the induced current by the inhomogeneous media. Let

$G(x, y)$ be the fundamental solution to the Helmholtz equation in the homogeneous background, that can be represented by (cf. [11, 12])

$$
(4) \qquad G(x, y) = \begin{cases} \dfrac{\mathrm{i}}{4} H_0^{(1)}(k|x - y|) & \text{for } N = 2; \\ \dfrac{1}{4\pi} \dfrac{\exp(\mathrm{i}k|x - y|)}{k|x - y|} & \text{for } N = 3 \end{cases}
$$

where $H_0^{(1)}$ refers to the Hankel function of the first kind and zeroth-order. With the help of the asymptotic properties of the fundamental solution G [12, Eqs. (2.14) and (3.63)], we have for $N = 2, 3$ that

$$
(5) \qquad u^s(x) = \frac{\exp(\mathrm{i}k|x|)}{|x|^{(N-1)/2}} \left\{ u^\infty(\hat{x}) + O(\frac{1}{|x|}) \right\} \qquad \text{as} \quad |x| \to \infty \,,
$$

with $\hat{x} = x/|x| \in \mathbb{S}^{N-1}$. The scattered near-field u^s and the far-field u^∞ in (5) has the following very convenient representations (cf. [12, Eqs.,(8.12) and (8.27)]):

$$
(6) \qquad u^s(x) \;\; = \;\; \int_D G(x, y) I(y) \, \mathrm{d}y \,,
$$

$$
(7) \qquad u^\infty(\hat{x}) \;\; = \;\; \int_D G^\infty(\hat{x}, y) I(y) \, \mathrm{d}y \,,
$$

where the far-field pattern associated with the fundamental solution G is given by

$$
(8) \qquad G^\infty(\hat{x}, y) = \begin{cases} \dfrac{\exp(\mathrm{i}\pi/4)}{\sqrt{8k\pi}} \exp(-\mathrm{i}k\hat{x} \cdot y), & N = 2; \\[2em] \dfrac{1}{4\pi} \exp(-\mathrm{i}k\hat{x} \cdot y), & N = 3. \end{cases}
$$

3. Direct sampling method using far-field data

In this section we shall derive the DSM using far-field data. Like many other sampling-type methods such as LSM, MUSIC and factorization methods [10, 24, 34], the essence of the DSM is to construct an indicator function which has significantly different behaviors inside and outside the scatterers, e.g., the indicator function of the LSM blows up outside the scatterer but remains finite within the scatterer. Let Γ be the surface where the near-field data is measured, Ω be a domain contained inside Γ such that the scatterer D lies in Ω. For any sampling point $x_p \in \Omega$, the indicator function of the DSM using near-field data is given by (cf. [21])

$$
(9) \qquad \Phi(x_p) = \frac{\left| \langle u^s, G(\cdot, x_p) \rangle_{L^2(\Gamma)} \right|}{\|u^s\|_{L^2(\Gamma)} \|G(\cdot, x_p)\|_{L^2(\Gamma)}}.
$$

For the motivation and derivations of (9) using near-field data we refer the reader to [21].

We are now going to derive an indicator function for the far-field data, a counterpart of (9) for the near-field data. To do so, we first derive the following key lemma about the L^2-correlation measure of the far-field data of two monopoles on the unit sphere.

Lemma 3.1. *For the far-field patterns $G^\infty(\hat{x}, y)$ associated with the fundamental solutions $G(x, y)$ (see (8) and (4)), the following correlation holds for any two points*

x_j and x_p in the sampling domain Ω:

$$(10) \qquad \int_{\mathbb{S}^{N-1}} G^\infty(\hat{x}, x_j)\overline{G^\infty}(\hat{x}, x_p)\,\mathrm{d}s(\hat{x}) = C\,\Im\left(G(x_p, x_j)\right)$$

where C is a constant depending only on the wave number k and the dimension N.

Proof. By the definition of G^∞, it is easy to verify that

$$(11) \qquad \int_{\mathbb{S}^{N-1}} G^\infty(\hat{x}, x_j)\overline{G^\infty}(\hat{x}, x_p)\,\mathrm{d}s(\hat{x}) = C_1 \int_{\mathbb{S}^{N-1}} \exp(\mathrm{i}k\hat{x} \cdot (x_p - x_j))\,\mathrm{d}s(\hat{x}),$$

where C_1 is a constant depending only on the wave number k and the dimension N.

We carry out the proof in two steps, one for $N = 2$, and the other for $N = 3$.

Step 1. For $N = 2$, (10) is a special case of Graf's addition theorem [1, Eq. (9.1.79)] by showing an integral representation of $J_n(kr)\exp(\mathrm{i}n\theta)$ for an integer n. To see this, we can write the right-hand side of (11) in polar coordinates

$$(12) \qquad \int_{\mathbb{S}^1} \exp(\mathrm{i}k\hat{x} \cdot (x_p - x_j))\,\mathrm{d}s(\hat{x}) = \int_{-\pi}^{\pi} \exp\left(\mathrm{i}k(x_p - x_j) \cdot \begin{pmatrix} \cos\theta \\ \sin\theta \end{pmatrix}\right)\,\mathrm{d}\theta.$$

It suffices to show that

$$(13) \qquad J_n(kr)\exp(\mathrm{i}n\theta) = \frac{(-\mathrm{i})^n}{2\pi} \int_{-\pi}^{\pi} \exp\left(\mathrm{i}kx \cdot \begin{pmatrix} \cos\phi \\ \sin\phi \end{pmatrix}\right)\exp(\mathrm{i}n\phi)\,\mathrm{d}\phi,$$

with $r = |x|$, and $x = (r\cos\theta, r\sin\theta)$. Therefore we can arrive at (10) in two dimensions, by setting $n = 0$, replacing x by $x_p - x_j$ in (13) and using the fact that

$$C\Im\left(G(x_p, x_j)\right) = \Im\left(\mathrm{i}H_0^{(1)}(k|x_p - x_j|)\right) = J_0(k|x_p - x_j|).$$

The formula (13) expresses regular cylindrical wave functions as a superposition of plane waves. To see (13), we first recall the Jacobi expansion [37, Eq. (22)]

$$(14) \qquad \exp(\mathrm{i}kr\cos\psi) = \sum_{m=-\infty}^{\infty} \mathrm{i}^m J_m(kr)\exp(\mathrm{i}m\psi).$$

By replacing ψ by $\theta - \phi$ in (14), then multiplying it by $\exp\left(-\mathrm{i}n(\theta - \phi)\right)$ and integrating over $(-\pi, \pi)$ with respect to ϕ we obtain

$$(15) \qquad \mathrm{i}^n J_n(kr) = \frac{1}{2\pi} \int_{-\pi}^{\pi} \exp\left(\mathrm{i}kr\cos(\theta - \phi)\right)\exp\left(-\mathrm{i}n(\theta - \phi)\right)\,\mathrm{d}\phi,$$

where we have employed the simple fact that $\int_{-\pi}^{\pi} \exp(\mathrm{i}n\psi)\,\mathrm{d}\psi = 2\pi$ for $n = 0$ and 0 for $n \neq 0$.

Now we can rewrite (15) as

$$(16) \qquad \mathrm{i}^n J_n(kr) = \frac{\exp\left(-\mathrm{i}n\theta\right)}{2\pi} \int_{-\pi}^{\pi} \exp\left(\mathrm{i}kr\cos\phi\cos\theta + r\sin\phi\sin\theta\right)\exp(\mathrm{i}n\phi)\,\mathrm{d}\phi,$$

which reproduces (13) by a simple rearrangement.

Step 2. For $N = 3$, we use the following special variant of the Funk-Hecke formula (cf. [12, Eq. 2.44] and [31, p. 29])

$$(17) \qquad \int_{\mathbb{S}^2} \exp(-\mathrm{i}kx \cdot \hat{z})Y_n(\hat{z})\,\mathrm{d}s(\hat{z}) = \frac{4\pi}{\mathrm{i}^n} j_n(k|x|)Y_n(\hat{x}), \quad x \in \mathbb{R}^3,\, r > 0$$

for spherical harmonics $Y_n(\cdot)$ of order n and spherical Bessel functions $j_n(\cdot)$ of order n. Now we set $n = 0$ and replace x by $x_p - x_j$ in (17). Being aware of the lowest

order spherical harmonics $Y_0(\hat{x}) \equiv 1/\sqrt{4\pi}$, which is a constant and thus can be dropped from both sides of the equation. Since $j_0(t) = \sin(t)/t$, we obtain that

$$C\Im\left(G(x_p, x_j)\right) = \Im\left(\frac{\exp(\mathrm{i}k|x_p - x_j|)}{k|x_p - x_j|}\right) = j_0(k|x_p - x_j|)$$

in three dimensions. This completes the proof. $\qquad\qquad\qquad\qquad\qquad\square$

Next, we divide the sampling domain Ω enclosing the scatterer D into a set of small elements $\{\tau_j\}$, i.e., squares in 2D or cubes in 3D. Then we approximate the integral relation (7) by the rectangular quadrature rule on each element:

$$(18) \qquad u^\infty(\hat{x}) = \int_\Omega G^\infty(\hat{x}, y) I(y)\, \mathrm{d}y \approx \sum_j w_j G^\infty(\hat{x}, y_j),$$

where the summation is over all elements τ_j which intersect the sampling domain Ω, the weight w_j is given by $|\tau_j| I_j$, with $|\tau_j|$ being the area/volume of the j-th element τ_j ($N = 2, 3$) and I_j the evaluation of $I(x)$ at the center of τ_j.

Now multiplying (18) by $\overline{G^\infty}(\hat{x}, x_p)$ for any sampling point $x_p \in \Omega$, then integrating over the unit sphere $\mathbb{S}^{N-1}$ and using (10), we obtain

$$(19) \qquad \int_{\mathbb{S}^{N-1}} u^\infty(\hat{x})\overline{G^\infty}(\hat{x}, x_p)\, \mathrm{d}s(\hat{x}) \approx C \sum_j w_j\, \Im\left(G(x_p, x_j)\right).$$

As we illustrate later (see Fig. 6), the right-hand side term $\Im\left(G(x_p, x_j)\right)$ above approaches a constant when x_p tends close to some point scatterer x_j and decays quickly as x_p moves away from x_j. This behavior motivates us with the following important indicator function for any sampling point $x_p \in \Omega$:

$$(20) \qquad \Phi^\infty(x_p) = \frac{\left|\langle u^\infty,\, G^\infty(\cdot, x_p)\rangle_{L^2(\mathbb{S}^{N-1})}\right|}{\|u^\infty\|_{L^2(\mathbb{S}^{N-1})} \|G^\infty(\cdot, x_p)\|_{L^2(\mathbb{S}^{N-1})}},$$

where the L^2-inner product occurring in the numerator is the integral given by the left-hand side of (19). In view of the singular behaviors of the fundamental solution $G(x, y)$ in (19), the indicator $\Phi^\infty(x_p)$ approaches the unity when x_p tends close to or lies within the medium scatterer and decays quickly as x_p moves away from the scatterer; see Fig. 6. This indicating behavior will serve as the key ingredient in our new DSM using far-field data.

We emphasize that the indicator function Φ^∞ in (20) was studied earlier in the orthogonality sampling method [33, 16], but derived from a different approach and motivation, and under a "smallness" assumption. As it has been seen, our theoretical foundation does not require such *smallness* restriction, thus makes it possible to explain partially why the DSM works also well for thin or long scatterers like rings and cracks. This is confirmed by numerical tests (see Examples 6 and 7 in Section 4).

Finally we make a short remark about computing the indicator function $\Phi^\infty(x_p)$ in (20). Clearly the computing is purely explicit and direct, involving only a cheap scalar product and a normalization operation, and it does not involve any matrix inversion and any solution process. Moreover, normalizations are quite cheap too. In fact we can easily see that the denominator in (20) is actually a constant and does not depend on the sampling point x_p, so it can be computed once for all sampling points. This is quite different from the indicator function (9) using near-field data.

Therefore, the DSM using far-field data is computationally much cheaper than its counterpart using near-field data.

4. Numerical examples

In this section, we will carry out a systematic evaluation of the performance of the DSM using the far-field data for some inverse scattering benchmark problems, including scatterers of obstacle, medium and crack types. In particular, we shall also present the numerical reconstructions by the DSM using the near-field data for most examples so that we may clearly see the comparisons and distinctions between these two different types of measurement data.

Let us first introduce our experiment settings. We shall present several examples to illustrate the applicability and robustness of the proposed method for determining the scatterers from both exact and noisy data. We shall take the unitary wavelength $\lambda = 1$, and the wave number $k = 2\pi$. When it is not mentioned, only one incident direction $d = (1, 1)^T/\sqrt{2}$ is employed in the examples; otherwise two incidents, $d_1 = (1, 1)^T/\sqrt{2}$ and $d_2 = (1, -1)^T/\sqrt{2}$, are used and mentioned explicitly. In all the examples, the scattered near-field data u^s is measured at 50 points uniformly distributed on a circle of radius 4λ centered at the origin, and the far-field pattern u^∞ is observed from 50 uniform distributed angles on the unit circle $\mathbb{S}^1$. The noisy data u^s_δ and u^∞_δ are generated point-wise by the formulae

$$(21) \qquad u^s_\delta = u^s(x) + \epsilon \zeta \max_x |u^s(x)| \quad \text{and} \quad u^\infty_\delta = u^\infty(x) + \epsilon \zeta \max_x |u^\infty(x)|$$

for both near-field and far-field data respectively, where ϵ refers to the relative noise level, and both real and imaginary parts of the noise ζ follow the standard normal distribution. Our near-field data are synthesized using the quadratic finite element discretization in the domain $(-6, 6)^2$ enclosed by a PML layer of width 1 to damp the reflection. Local adaptive refinement scheme within the inhomogeneous scatterer is adopted to enhance the resolution of the scattered wave. The far-field data are generated approximately by the integral representation [12, Eq. (3.64)] along the circle centered at the origin with radius 5 using the composite Simpson's rule:

$$\int_0^{2\pi} 5f(5, \theta) \, \mathrm{d}\theta \approx \frac{\pi}{15} \sum_0^{24} (f_{2i} + 4f_{2i+1} + f_{2i+2})$$

where $f(r, \theta)$ is the integrand of Eq. (3.64) in [12] in the polar form and f_j is the value of f evaluated at the j-th quadrature node $(r, \theta) = (5, 2j\pi/50)$, $j = 0, 1, \ldots, 50$. To ensure the sufficient accuracy of the far-field data, we refine the mesh successively till the relative maximum error of the data from two successive meshes is below 0.1%. The indicator function value is normalized between 0 and 1, and the sampling domain is fixed to be $\Omega = [-2\lambda, 2\lambda]^2$, which is divided into small squares of equal width $h = 0.01\lambda$. The contour plot of the indicator function value will be displayed as an estimate to the profiles of unknown scatterers. For multiple incident waves with directions $d_1, d_2, \ldots, d_\nu$, we take the maximum of all indicator function values point-wise:

$$(22) \qquad \Phi^\infty(x_p) = \max \left\{ \Phi^\infty(x_p; d_1), \, \Phi^\infty(x_p; d_2), \, \cdots, \Phi^\infty(x_p; d_\nu) \right\},$$

where $\Phi^\infty(x_p; d_l)$, $l = 1, 2, \ldots, \nu$, is the indicator function defined by (20) associated with the l-th incident direction d_l. We denote the DSM using near-field and far-field data by DSM(n) and DSM(f), respectively, for sake of comparisons of their
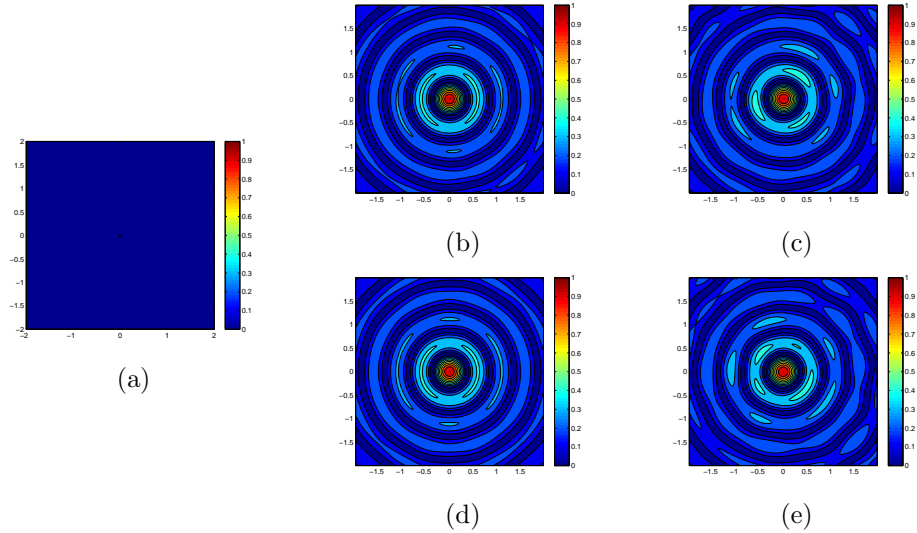
FIGURE 1. Example 1: (a) true scatterer; Reconstruction results using (b) exact near-field data, (c) noisy near-field data with $\epsilon = 20\%$, (d) exact far-field data, (e) noisy far-field data with $\epsilon = 20\%$.

performances. We shall carry out three groups of benchmark problems: medium scatterer, obstacle scatterer, and crack scatterer.

DSM FOR MEDIUM SCATTERERS. We first test the four examples from [21], but using both near-field and far-field data to compare the performances of two different types of data.

Example 1 (A singular point medium). The example considers one square scatterer of width 0.02λ located at the origin, with coefficient η of the scatterer being 1.

This point scatterer identification is a standard benchmark problem. The contour plots using the DSM(n) and DSM(f) are shown in Figure 1. With only one incident wave probing, the location of the point scatterer is accurately positioned even if the data is severely distorted. We observe similar behavior of both indicator functions using near-field and far-field data. Both DSM(n) and DSM(f) can locate the position of the "point" scatterer in an accurate and stable way. The presence of noise level up to 20% in both measurement data has little effects on the indicator functions.

Example 2 (Well-separated medium scatterers) Two square scatterers of side length 0.3λ, located at $(-0.8\lambda, -0.7\lambda)$ and $(0.3\lambda, 0.8\lambda)$ respectively, are considered, both with coefficient η being 1.

This example verifies that the DSM can capture multiple sources. The indicating contour plots of the DSM using near-field and far-field data are shown in Figure 2. Both DSM(n) and DSM(f) are able to identify the location of both scatterers even if the measured data is significantly perturbed. Through studying the contrast of the indicator contours of medium scatterers with respect to the surrounding background medium, one can choose the cut-off value ranging from 0.7 to 0.8 to truncate the profiles of the two scatterers. Choosing a large cut-off value helps reducing those misleading spurious medium scatterers, see yellow patches in Figure 2(b)-(e).
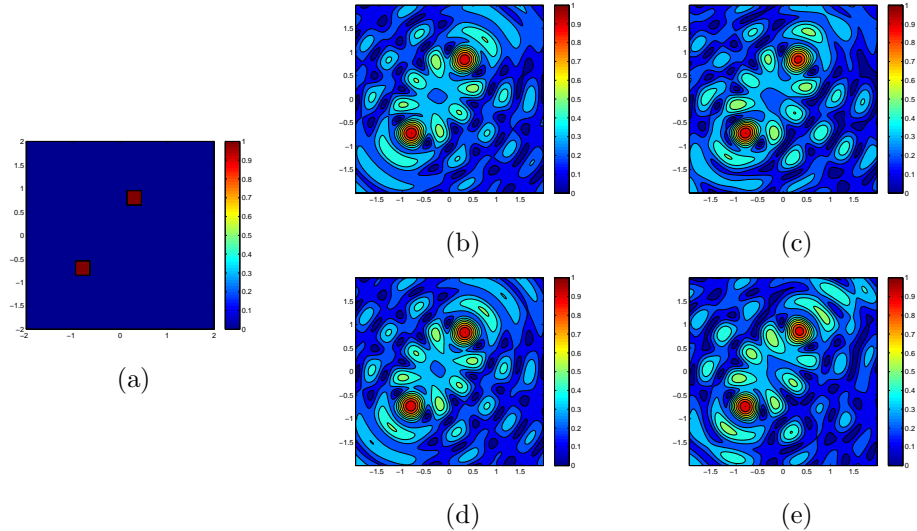
(a)   (b)   (c)

(d)   (e)

FIGURE 2. Example 2: (a) true scatterer; reconstruction results using (b) exact near-field data, (c) noisy near-field data with $\epsilon = 20\%$, (d) exact far-field data, (e) noisy far-field data with $\epsilon = 20\%$.

Example 3 (Two close medium scatterers). Here the same setting as Example 2 is laid out, except that the two scatterers are now moved to $(-0.25\lambda, 0)$ and $(0.25\lambda, 0)$, respectively.

This example investigates the resolution limit when the DSM can separate multiple sources. The results of near-field case and far-field case are shown in Figure 3. Both the DSM(n) and DSM(f) can separate these two close medium scatterers well. The location and size of the scatterers agrees well with the true ones even under large noise. When we further reduce the distance between those two scatterers (less than half a wave length), DSM cannot separate the two scatterer any longer, which is consistent with the Heisenberg uncertainty principle.

Example 4 (A ring-shaped medium scatterer). We consider a ring-shaped square scatterer located at the origin, with the outer and inner side lengths being 0.6λ and 0.4λ respectively and the coefficient η being 1. Two incident directions $d_1 = \frac{1}{\sqrt{2}}(1, 1)^T$ and $d_2 = \frac{1}{\sqrt{2}}(1, -1)^T$ are employed. The reconstruction results using near-field and far-field data are shown in Figures 4 and 5 respectively.

This is a rather challenging task to estimate the profile of the scatterer. We see that the DSM(f) has similar performance to the DSM(n). One single incident wave is inadequate to revolve full features of the scatterer. Using two incident waves, The four corners of the square ring is correctly labeled by the peaks of the superimposed indicator function in Figure 4(d), (g) and Figure 5(c), (f).

From the above four examples, we see that the DSM(f) has similar performance as the DSM(n). Both methods work stably and can tolerate strong noise. These estimated locations and index values can serve as good initial guesses for further reconstructions of more accurate locations and inhomogeneity profile $\eta(x)$ of scatterers through computationally much more demanding resolution processes such as nonlinear optimizations.
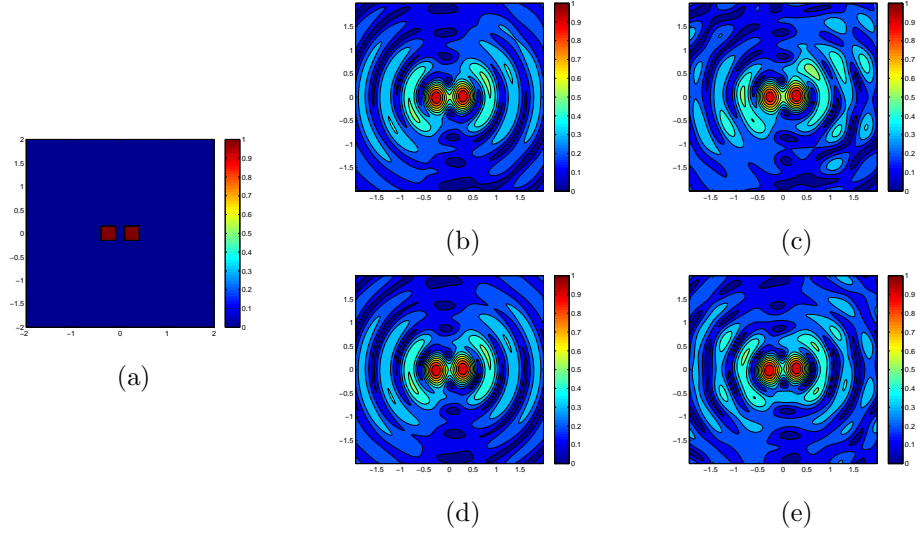
Figure 3. Example 3: (a) true scatterer; reconstruction results using (b) exact near-field data, (c) noisy near-field data with $\epsilon = 20\%$, (d) exact far-field data, (e) noisy far-field data with $\epsilon = 20\%$.

Physical interpretation. Before we study more challenging examples, we try to provide a physical justification of the DSM using both near-field and far-field data based on some numerical observations.

Let us first consider the key factor $\Im\left(G(x_p, x_j)\right)$ in the correlation measure (19), which can be explicitly written (with an appropriate scaling factor) as:

$$(23) \qquad C_N \Im\left(G(x_p, x_j)\right) = \begin{cases} J_0(k|x_j - x_p|), & N = 2; \\[2mm] \dfrac{\sin(k|x_j - x_p|)}{k|x_j - x_p|}, & N = 3, \end{cases}$$

where $C_N = 4$ and 4π for $N = 2$ and 3, respectively. Figure 6 shows that the leading term $C_N \Im\left(G(x_p, x_j)\right)$ of the correlation measure achieves the maximum when x_p approaches x_j, and decays quickly as the distance between them increases.

Let us now first explain the DSM using far-field data. From Figure 6, it can be seen clearly that there is much stronger pattern correlation between $u^\infty(\hat{x})$ and $G^\infty(\hat{x}, x_p)$ in (19) when $r = |x_p - x_j|$ is small, namly the sampling point x_p is sufficiently close to the center x_j of some inhomogeneous sampling element where I_j does not vanish due to the non-vanishing $\eta(x_j)$. Let us take Example 1 to illustrate this key relation. We plot in Figure 7 the pointwise complex ratio of the far field data $u^\infty(\hat{x})$ to the far field pattern $G^\infty(\hat{x}, x_p)$ of the fundamental solutions located at the sampling point x_p being the origin. This complex ratio is computed with respect to 50 observation angles in $[0, 2\pi]$ in the polar form with its polar radius and phase angle depicted in the left and right plots, respectively. It can be easily observed that both the polar radius and the phase angle in Figure 7 approaches some constants. In other words, $u^\infty(\hat{x})$ and $G^\infty(\hat{x}, x_p)$ are almost linear dependent with each other.
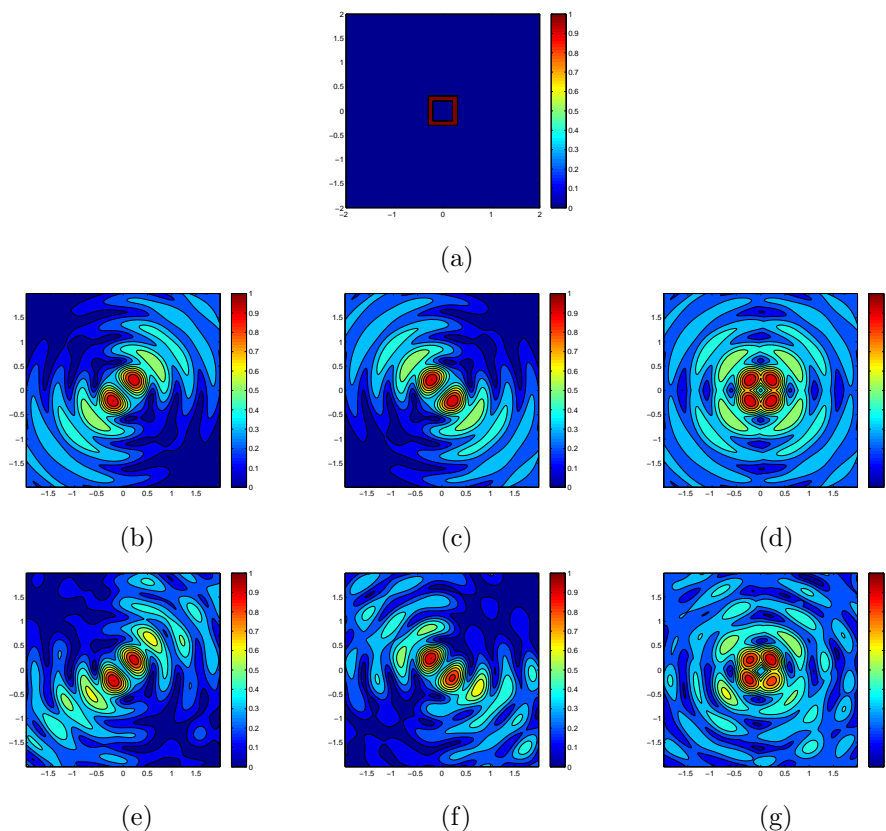
Figure 4. Example 4: (a) true scatterer; reconstruction results using exact near-field data (b), (c), (d), and noisy data (e), (f), (g) with $\epsilon = 20\%$; incident directions d_1, d_2 and (d_1, d_2) used respectively for (b) & (e), (c) & (f) and (d) & (g).

For multi-component small-scaled medium scatterers with sufficiently large distance between each other, multiple scattering is weak and thus ignored, so the exact scattered wave field u^s can be approximated by its reduced counterpart, namely a superposition of small point sources induced by the incident plane wave illuminating the scatterers. Thanks to the superposition principle of the wave phenomena, some scattered wave by an individual small medium scatterer shares common decay pattern with $G(x, x_p)$ when x_p falls within the inhomogeneous medium, which leads to the parallelism of some component of $u^\infty(\hat{x})$ and $G^\infty(\hat{x}, x_p)$ in the trace space on $\mathbb{S}^{N-1}$ as shown in Figure 7. Physically speaking, it amounts to exciting point sources when a plane wave impinges on some small-scaled media (size of media is less then a half wavelength). Then the far-field pattern $G^\infty(\hat{x}, x_p)$ of the fundamental solution becomes a major component of the far-field u^∞ when x_p is located within the scatterer. Therefore, if the indicator function $\Phi^\infty(x_p)$ approaches 1 for some sampling point x_p, it is plausible to claim that x_p is within the scatterer obstacle or medium.

The reasoning for the DSM using near-field data can be viewed as a direct consequence of that of its far-field version. Again we use Example 1 for illustration
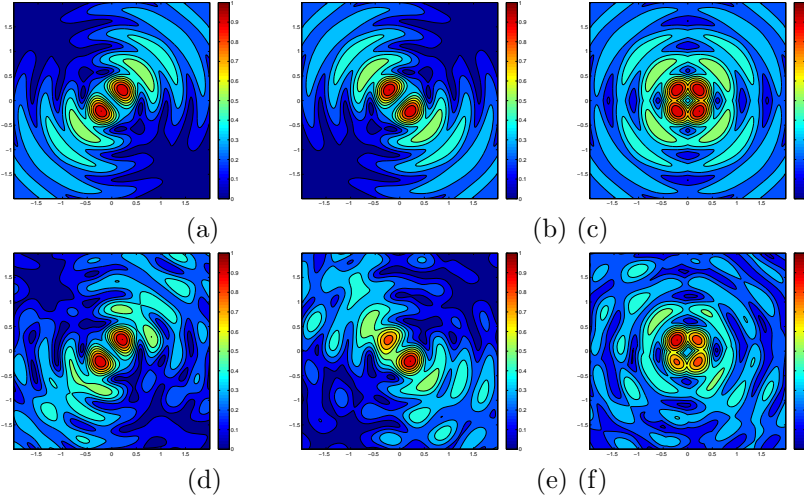
FIGURE 5. Example 4: reconstruction results using exact far-field data (a), (b), (c), and noisy data (d), (d), (f) with $\epsilon = 20\%$; incident directions d_1, d_2 and (d_1, d_2) used respectively for (a) & (d), (b) & (e) and (c) & (f).
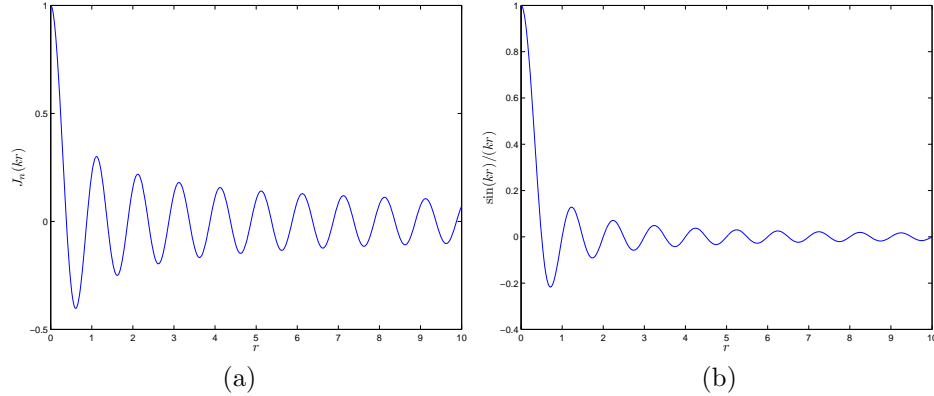

FIGURE 6. Decay patterns of $C_N \Im (G(x_p, x_q))$ as $r = |x_p - x_q|$ increases in two dimensions (a) and three dimensions (b) when $k = 2\pi$.

by taking the sampling point x_p to be the origin. Under the assumption of sufficiently large distance between the measurement surface Γ and the small scatterer inside (normally four or five times the wavelength), the traces of $u^s(x)$ and $G(x, x_p)$ on Γ depend approximately linearly on their asymptotic amplitudes $u^\infty(\hat{x})$ and $G^\infty(\hat{x}, x_p)$, respectively, up to some complex scaling factors. This can be verified by checking the pointwise complex ratio of $u^s(x)$ to $u^\infty(\hat{x})$ and that of $G(x, x_p)$ to $G^\infty(\hat{x}, x_p)$, respectively, as showin in Figure 8. By recalling the nearly linear dependence of $u^\infty(\hat{x})$ and $G^\infty(\hat{x}, x_p)$ and the transitivity of the three linear approximations aforementioned, it leads naturally to the nearly linear dependence of the
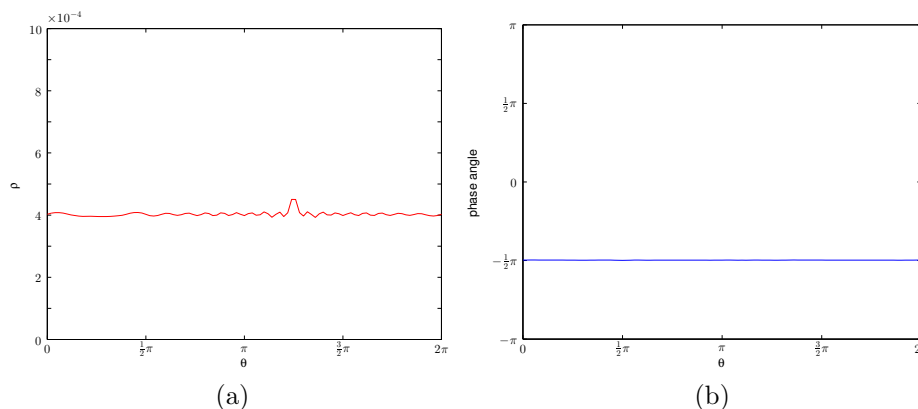
FIGURE 7. Pointwise complex ratio ((a) polar radius; (b) phase angle) of $u^\infty(\hat{x})$ to $G^\infty(\hat{x}, x_p)$ versus all the observation angle θ. Here x_p is chosen to be the origin, the center of the small inhomogeneous scatterer in Example 1.

traces of $u^s(x)$ and $G(x, x_p)$ on Γ, which explain the effectiveness of the indicator function (9) in [21].

For multi-component scatterers, as in the far field case, the scattering field u^s may well reduce to a superposition of small point sources induced by the incident plane wave illuminating the scatterers plus some high order terms due to the multiple scattering. When the sampling point x_p falls within a medium scatterer, one can obtain a nearly linear dependence of a significant component of the scattering field u^s on the trace of the point source $G(x, x_p)$ restricted on Γ. After normalization, such physical correlation of the near fields u^s and $G(x, x_p)$ leads to a fairly large value (nearly one) of the indicator function $\Phi(x_p)$ for the sampling point x_p.

DSM for mixed obstacle and medium scatterers. The next example considers a mixed scatterer composed of an obstacle and an inhomogeneous medium with variable material coefficient.

Example 5 (A mixed scatterer with obstacle and medium). The example considers two square scatterers of side length 0.3λ. The two scatterers are located at $(-0.8\lambda, -0.7\lambda)$ (a sound-soft obstacle) and $(0.3\lambda, 0.8\lambda)$ (an inhomogeneous medium), respectively. The lower left one is an obstacle, which is excluded from the domain and denoted by a white square. We vary the coefficient η in the upper right inhomogeneous square to study the wave interaction of obstacle and medium scatterers.

This example verifies the capability of both types of DSMs to identify obstacles and also shows the condition under which the DSM can identify both obstacles and media. The results for $\eta = 1$ and $n^2 = 10 + 10i$ using the DSM(n) and DSM(f) are shown in Figures 9 and 10 respectively. For $\eta = 1$, it amounts to a refractive index $n = \sqrt{1 + 1/(2\pi)^2}$ for the right upper square medium scatter, which is very close to the background medium with unit refractive index. The scattering effect of the inhomogeneous medium scatterer is so small compared to the scattered wave due to the obstacle square. Therefore, one can only locate correctly the position of the obstacle and loses track of the information of the inhomogeneous medium scatterer.
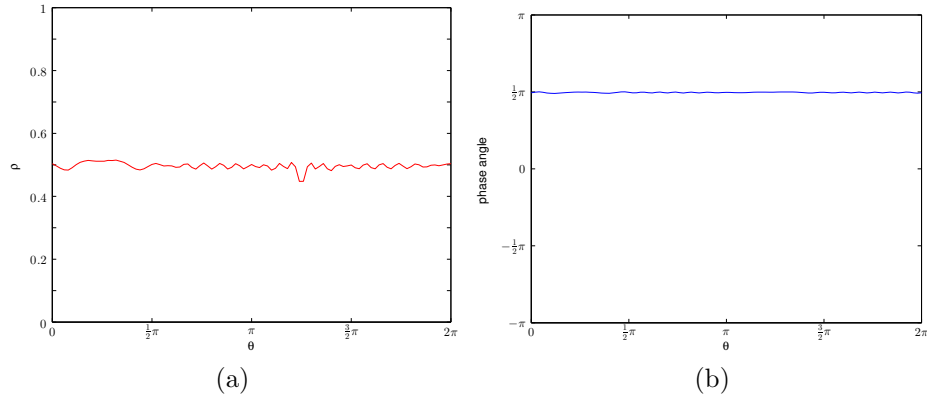
Complex ratio ((a) polar radius; (b) phase angle) of $u^s(x)$ to $u^\infty(\hat{x})$ versus the observation angle θ.
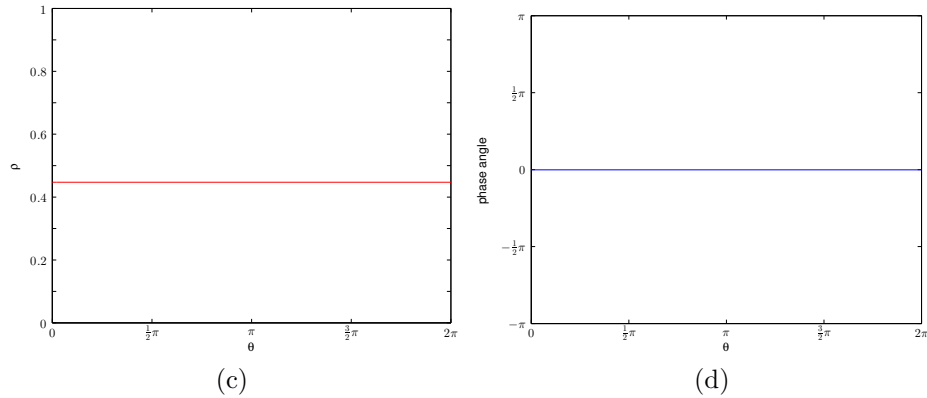
Complex ratio ((c) polar radius; (d) phase angle) of $G(x, x_p)$ to $G^\infty(\hat{x}, x_p)$ versus the observation angle θ.

FIGURE 8. Illustration of approximately linear dependence of the traces of $u^s(x)$ and $G(x, x_p)$ on Γ on their asymptotic amplitudes $u^\infty(\hat{x})$ and $G^\infty(\hat{x}, x_p)$, respectively. Here x_p is chosen to be the origin, the center of the small inhomogeneous scatterer in Example 1.

However, when we increase the refractive index n^2 to be $10 + 10i$, the multiple scattering interaction of the scattered wave field due to the obstacle and medium scatterers becomes more evident. Only in such circumstances the location of the medium scatterer emerges gradually as a red patch in the correct northeast location. In other words, the DSM performs well for mixed types of scatterers under the assumption that the interaction of scattered wave due to each individual scatterer (be it an obstacle or a medium scatterer) must be strong enough. Such good performance is quite robust with respect to large noise level.

DSM FOR CRACKS. Now we are going to test two examples with cracks and demonstrate an interesting and promising application of the DSM to such an important scattering scenario.
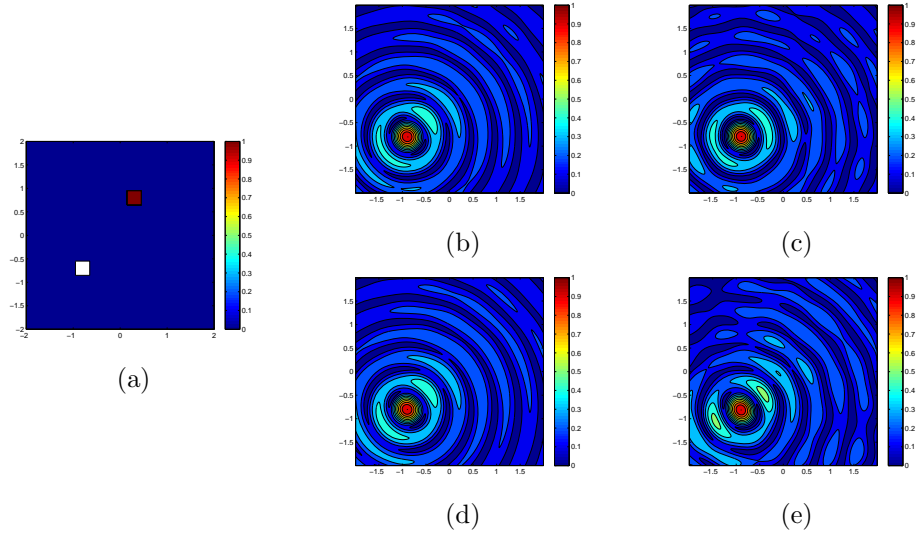
FIGURE 9. Example 5 with $\eta = 1$: (a) true scatterer; reconstruction results using (b) exact near-field data, (c) noisy near-field data with $\epsilon = 20\%$, (d) exact far-field data, (e) noisy far-field data with $\epsilon = 20\%$.
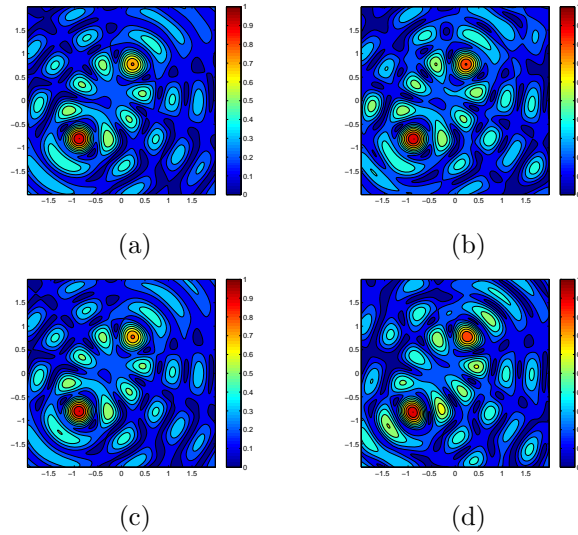

FIGURE 10. Example 5 with $n^2 = 10 + 10i$, : reconstruction results using (a) exact near-field data, (b) noisy near-field data with $\epsilon = 20\%$, (c) exact far-field data, (d) noisy far-field data with $\epsilon = 20\%$.
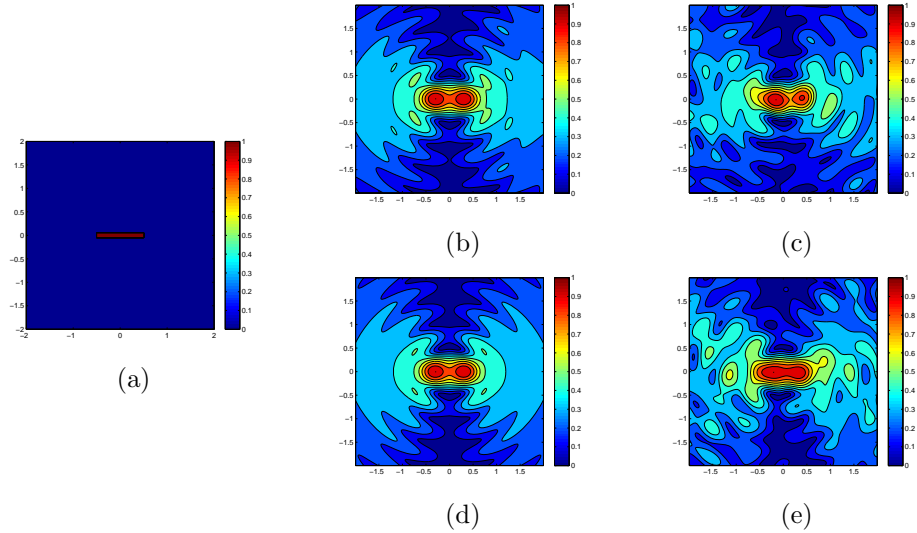
Figure 11. Example 6: (a) true crack scatterer; reconstruction results using (b) exact near-field data, (c) noisy near-field data with $\epsilon = 20\%$, (d) exact far-field data, (e) noisy far-field data with $\epsilon = 20\%$.

Example 6 (A horizontal crack). This example considers a thin crack of thickness 0.1λ, centered at the origin and parallel to the x-axis lying in the middle of the domain with length 1. The medium scatterer with coefficient $\eta = 1$ is illuminated by a horizontal incident plane wave, see Figures 11(a) for the configuration.

Cracks are the most illusive scatterer type to be identified as it has a very small thickness, and it is non-trivial even with the data from multiple incident directions. The results using the near-field and far-field data from just one incident field are shown in Figure 11.

In the noise-free cases, both DSM(n) and DSM(f) can successfully determine the location and length for the crack, and the identified geometry is roughly a red long bar with correct length. It is important to observe that the DSM also works for this difficult example with one incident, even with large noise, say $\epsilon = 20\%$; see Figure 11 (c), (e). But in this case, the DSM(f) performs better than the DSM(n), which seems to break the crack into two pieces.

Example 7 (An L-shape crack). The example considers an L-shape crack with thickness 0.1λ and length 2λ. The coefficient η in the inhomogeneous region is 1.

This L-shaped crack is more challenging than the crack in Example 6. We use the incident wave along direction $d_2 = (1, -1)^T/\sqrt{2}$ and the reconstruction is given in Figure 12. One can see that an L-shaped dark yellow bar is identified by choosing the cut-off value about 0.7 in the noise-free case for both DSM(n) and DSM(f). But with 20% noise, the DSM(f) provides a much better profile than the DSM(n) in terms of the length and connectedness of the crack.

Finally we test with two incident wave directions d_1 and d_2, and report the results in Figure 13. One can see that both DSM(n) and DSM(f) can yield significantly enhanced images than those obtained using a single wave in direction d_1 or d_2.
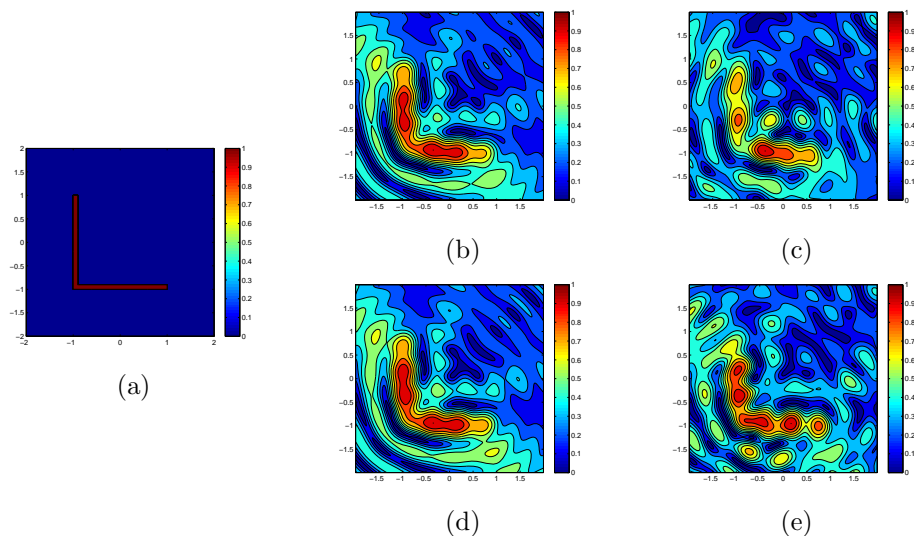
FIGURE 12.   Example 7 with incident direction $d_2 = (1, -1)^T/\sqrt{2}$: (a) true L-shape crack scatterer; reconstruction results using (b) exact near-field data, (c) noisy near-field data with $\epsilon = 20\%$, (d) exact far-field data, (e) noisy far-field data with $\epsilon = 20\%$.

DSM(n) using two incident waves: from left to right, noise level is 0, 5%, 10%, 20%.

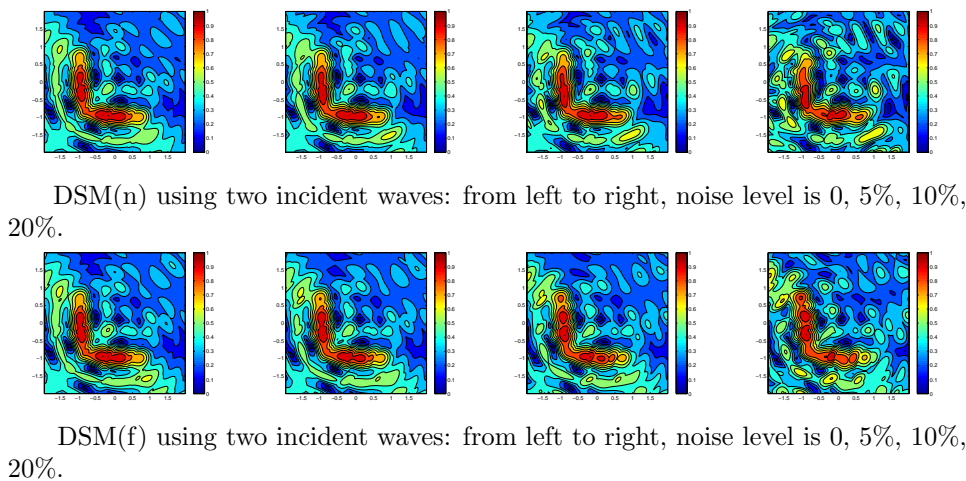DSM(f) using two incident waves: from left to right, noise level is 0, 5%, 10%, 20%.

FIGURE 13. Numerical results of Example 7 using two incident directions d_1 and d_2 .

Moreover, the recovered L-shaped geometry degenerates rather slowly as we increase the noise level from 5% to 20%, see Figure 13. This example demonstrates the robustness and effectiveness of the DSM as a potential promising technique for crack detections.

5. CONCLUDING REMARKS

A systematic evaluation of the performance of the DSM using both far-field data and near-field data has been carried out for some inverse scattering benchmark problems, such as scatterers of obstacle, medium and crack types. The numerical simulations have demonstrated the robustness and effectiveness of the DSM to identify the locations of obstacles, inhomogeneity media, as well as thin cracks, with just one or two incident directions. An important advantage of the DSM is its tolerance against large noise in the observation data.

The DSM method involves only simple operations like inner products, without any inversion or solution process required, so it is computationally very cheap, hence not intended for an accurate reconstruction of unknown scatterers and their physical inhomogeneity. As it is cheap and works with the data from even one incident field, it can serve as a fast, simple and effective numerical tool for locating reliable approximate positions of unknown scatterers. The reconstructed shapes of scatterers and the final numerical indicator function values by DSM may then serve as a good initial guess for any other more advanced method to achieve a more accurate estimate of the scatterer shapes and the inhomogeneity distribution. In addition, with the reliable location of each individual scatterer component extracted by the DSM, one may start with a much smaller sampling region in a more accurate but computationally much more demanding method (see, e.g., [4, 12, 19, 22]). Considering the severe ill-posedness of the inverse scattering problems, the reduction of the sizes of the initial sampling regions for unknown scatterers may save us an essential fraction of the computational efforts in the entire reconstruction process.

ACKNOWLEDGEMENTS

REFERENCES

[1] M. Abramowitz and I. A. Stegun, eds., "Handbook of Mathematical Functions," Dover, NewYork, 1965.

[2] G. Alessandrini and L. Rondi, *Determining a sound-soft polyhedral scatterer by a single far-field measurement*, Proc. Am. Math., **6** (2005), pp. 1685–1691.

[3] H. Ammari and H. Kang, "Reconstruction of Small Inhomogeneities from Boundary Measurements," vol. 1846 of Lecture Notes in Mathematics, Springer-Verlag, Berlin, 2004.

[4] G. Bao and P. Li, *Inverse medium scattering for the Helmholtz equation at fixed frequency*, Inverse Problems, **21** (2005), pp. 1621–1641.

[5] L. Beilina and M. V. Klibanov, "Approximate Global Convergence and Adaptivity for Coefficient Inverse Problems," Springer, New York, 2012.

[6] J. Buchanan, R. Gilbert, A. Wirgin, and Y. Xu, "Marine Acoustics: Direct and Inverse Scattering of Waves," SIAM, Philadelphia, 2004.

[7] F. Cakoni, D. Colton, and P. Monk, "The Linear Sampling Method in Inverse Electromagnetic Scattering," Philadelphia: SIAM, 2011.

[8] X. Chen and Y. Zhong, *MUSIC electromagnetic imaging with enhanced resolution for small inclusions*, Inverse Problems, **25** (2009), 015008 (11pp).

[9] M. Cheney, *The linear sampling method and the MUSIC algorithm*, Inverse Problems, **17** (2001), pp. 591–595.

[10] D. Colton and A. Kirsch, *A simple method for solving inverse scattering problems in the resonance region*, Inverse Problems, **12** (1996), pp. 383–393.

[11] D. Colton and R. Kress "Integral Equation Methods in Scattering Theory," John Wiley & Sons, New York, 1983.

[12] D. Colton and R. Kress, "Inverse Acoustic and Electromagnetic Scattering Theory," Springer, 1998.

[13] D. Colton and B. D. Sleeman, *Uniqueness theorems for the inverse problem of acoustic scattering*, IMA Journal of Applied Mathematics, **31** (1983), pp. 253–259.

[14] A. Devaney, *Super-resolution processing of multi-static data using time-reversal and MUSIC*, J. Acoust. Soc. Am., accepted, http:www.ece.neu.edufacultydevaney/preprintspaper02n_00.pdf.

[15] J. Elschner and M. Yamamoto, *Uniqueness in determining polyhedral sound-hard obstacles with a single incoming wave*, Inverse Problems, **24** (2008), 035004 (7pp).

[16] R. Griesmaier, *Multi-frequency orthogonality sampling for inverse obstacle scattering problems*, Inverse Problems, **27** (2011), 085005 (23pp).

[17] F. K. Gruber, E. A. Marengo, and A. J. Devaney, *Time-reversal imaging with multiple signal classification considering multiple scattering between the targets*, J. Acoust. Soc. Am., **115** (2004), 3042 (6pp).

[18] M. Hanke, *One shot inverse scattering via rational approximation*, SIAM J. Imaging Sciences, **5** (2012), pp. 465–482.

[19] T. Hohage, *On the numerical solution of a three-dimensional inverse medium scattering problem*, Inverse Problems, **17** (2001), pp. 1743–1763.

[20] S. Hou, K. Solna, and H. Zhao, *A direct imaging algorithm for extended targets*, Inverse Problems, **22** (2006), pp. 1151–1178.

[21] K. Ito, B. Jin, and J. Zou, *A direct sampling method to an inverse medium scattering problem*, Inverse Problems, **28** (2012), 025003 (10pp).

[22] K. Ito, B. Jin, and J. Zou, *A two-stage method for inverse medium scattering*, Technical Report 2012-09 (398), Department of Mathematics, Chinese University of Hong Kong, 2012. Also available at http://arxiv.org/abs/1205.4277; arXiv:1205.4277v1.

[23] A. Kirsch, *Characterization of the shape of a scattering obstacle using the spectral data of the far field operator*, Inverse Problems, **14** (1998), pp. 1489–1511.

[24] A. Kirsch and N. Grinberg, "The Factorization Method for Inverse Problems," New York : Oxford University Press, 2008.

[25] R. Kohn, D. Onofrei, M. Vogelius, and M. Weinstein, *Cloaking via change of variables for the helmholtz equation*, Comm. Pure Appl. Math., **63** (2010), pp. 973–1016.

[26] J. Li, H. Liu, and H. Sun, *Enhanced approximate cloaking by SH and FSH lining*, Inverse Problems, **28** (2012), 075011 (21pp).

[27] H. Liu, and H. Sun, *Enhanced near-cloak by FSH lining*, Journal de Mathematiques Pures et Appliquees, to appear, arXiv:1110.0752v2.

[28] H. Liu, M. Yamamoto and J. Zou, *Reflection principle for the maxwell equations and its application to inverse electromagnetic scattering*, Inverse Problems, **23** (2007), pp. 2357–2366.

[29] H. Liu, H. Zhang, and J. Zou, *Recovery of polyhedral scatterers by a single electromagnetic far-field measurement*, J. Math. Phy., **50** (2009), 123506 (10pp).

[30] H. Liu and J. Zou, *Uniqueness in an inverse acoustic obstacle scattering problem for both sound-hard and sound-soft polyhedral scatterers*, Inverse Problems, **22** (2006), pp. 515–524.

[31] C. Müller, "Analysis of spherial symmetries in Eulidean spaes," Springer, New York, 1997.

[32] R. Potthast, *A survey on sampling and probe methods for inverse problems*, Inverse Problems, **22** (2006), pp. R1–R47.

[33] R. Potthast, *A study on orthogonality sampling*, Inverse Problems, **26** (2010), 074015 (17pp).

[34] R. Schmidt, *Multiple emitter location and signal parameter estimation*, IEEE Trans. Antennas Propag., **34** (1986), pp. 276–280.

[35] C. G. Someda, "Electromagnetic Waves," Boca Raton, FL: CRC Press, 2 ed., 2006.

[36] P. M. van den Berg, A. L. van Broekhoven, and A. Abubakar, *Extended contrast source inversion*, Inverse Problems, **15** (1999), pp. 1325–1343.

[37] G. N. Watson, "A Treatise on the Theory of Bessel Functions," CambridgeUniversityPress, Cambridge, 2 ed., 1944.

E-mail address: li.jz@sustc.edu.cn

E-mail address: zou@math.cuhk.edu.hk